



**HAL**  
open science

## Submillimetre dust polarization and opacity in the HD163296 protoplanetary ring system

W. R. F. Dent, C. Pinte, P. C. Cortes, F. Ménard, A. Hales, E. Fomalont, I.  
de Gregorio-Monsalvo

► **To cite this version:**

W. R. F. Dent, C. Pinte, P. C. Cortes, F. Ménard, A. Hales, et al.. Submillimetre dust polarization and opacity in the HD163296 protoplanetary ring system. *Monthly Notices of the Royal Astronomical Society: Letters*, 2019, 482, pp.L29-L33. 10.1093/mnrasl/sly181 . insu-03704143

**HAL Id: insu-03704143**

**<https://insu.hal.science/insu-03704143>**

Submitted on 24 Jun 2022

**HAL** is a multi-disciplinary open access archive for the deposit and dissemination of scientific research documents, whether they are published or not. The documents may come from teaching and research institutions in France or abroad, or from public or private research centers.

L'archive ouverte pluridisciplinaire **HAL**, est destinée au dépôt et à la diffusion de documents scientifiques de niveau recherche, publiés ou non, émanant des établissements d'enseignement et de recherche français ou étrangers, des laboratoires publics ou privés.

# Submillimetre dust polarization and opacity in the HD163296 protoplanetary ring system

W. R. F. Dent,<sup>1</sup>★ C. Pinte<sup>2,3</sup>, P. C. Cortes,<sup>1,4</sup> F. Ménard,<sup>3</sup> A. Hales,<sup>1,4</sup> E. Fomalont<sup>1,4</sup> and I. de Gregorio-Monsalvo<sup>1</sup>

<sup>1</sup>ALMA JAO, Alonso de Córdova 3107, Casilla 763 0355, Santiago, Chile

<sup>2</sup>Monash Centre for Astrophysics (MoCA) and School of Physics and Astronomy, Monash University, Clayton Vic 3800, Australia

<sup>3</sup>University Grenoble Alpes, CNRS, IPAG, F-38000 Grenoble, France

<sup>4</sup>National Radio Astronomy Observatory, 520 Edgemont Road, Charlottesville, VA 22903-2475, USA

Accepted 2018 September 23. Received 2018 September 23; in original form 2018 July 1

## ABSTRACT

We present ALMA images of the sub-mm continuum polarization and spectral index of the protoplanetary ringed disc HD163296. The polarization fraction at 870  $\mu\text{m}$  is measured to be  $\sim 0.9$  per cent in the central core and generally increases with radius along the disc major axis. It peaks in the gaps between the dust rings, and the largest value ( $\sim 4$  per cent) is found between rings 1 and 2. The polarization vectors are aligned with the disc minor axis in the central core, but become more azimuthal in the gaps, twisting by up to  $\pm 9^\circ$  in the gap between rings 1 and 2. These general characteristics are consistent with a model of self-scattered radiation in the ringed structure, without requiring an additional dust alignment mechanism. The 870/1300  $\mu\text{m}$  dust spectral index exhibits minima in the centre and the inner rings, suggesting these regions have high optical depths. However, further refinement of the dust or the disc model at higher resolution is needed to reproduce simultaneously the observed degree of polarization and the low spectral index.

**Key words:** submillimetre: planetary systems – physical data and processes: polarization.

## 1 INTRODUCTION

Images of protoplanetary discs, now being routinely obtained on spatial scales of tens of au, are showing that dust frequently lies in concentric rings (e.g. ALMA Partnership et al. 2015). Polarized emission at mm wavelengths is a way to further constrain both the disc physics and dust properties. Originally regarded as a tracer of non-spherical magnetically aligned grains, it was later recognized that self-scattering of mm radiation can be important; the polarization could then inform us about disc geometry, optical depths, and dust geometry (Kataoka et al. 2016a; Yang et al. 2017). In the disc mid-plane, collisions with the gas can suppress magnetic field alignment, although non-spherical grains may still be aligned with the dominant local radiation field through radiative torque (Tazaki, Lazarian & Nomura 2017). The spatial structure of polarized emission is critical to distinguish these mechanisms, but this requires well-resolved images.

The near-face-on transition disc HD142527 showed predominantly radial polarization vectors consistent with self-scattering, with some outer regions of azimuthal orientation, possibly from radiatively aligned grains (Kataoka et al. 2016b). At 3 mm, the more

inclined multiringed disc of HL Tau showed azimuthal polarization vectors consistent with radiative alignment (Kataoka et al. 2017). However, at 870  $\mu\text{m}$  the vectors are more parallel and aligned along the minor axis, suggesting that scattering may dominate. Intermediate wavelengths (1.3 mm) show a mixture of the two components (Stephens et al. 2017). The extended full disc IM Lup also shows vectors aligned more with the minor axis, and was interpreted as scattered emission (Hull et al. 2018). Inclined younger Class 0/I discs also tend to show polarization vectors aligned with the minor axis (Cox et al. 2018; Harris et al. 2018; Lee et al. 2018)

The target for this study, HD163296, is a well-studied isolated Herbig Ae star, with a bright, extended disc. Lying at a distance of 105 pc,<sup>1</sup> it is classified as spectral type A2Ve, of age 5 Myr (Montesinos et al. 2009). In CO gas, the disc extends to  $\sim 450$  au, but appears only half this size when observed in mm dust (de Gregorio-Monsalvo et al. 2013). Detailed fits indicated that the dust lies in rings (Zhang et al. 2016), subsequently confirmed by higher resolution mm observations that showed three concentric structures (Isella et al. 2016). The innermost of these is traced in near-infrared scattered light (Monnier et al. 2017; Muro-Arena et al. 2018). Early

\* E-mail: [wdent@alma.cl](mailto:wdent@alma.cl)

<sup>1</sup>Sizes and luminosities in this paper have been revised based on the GAIA DR2 parallax.

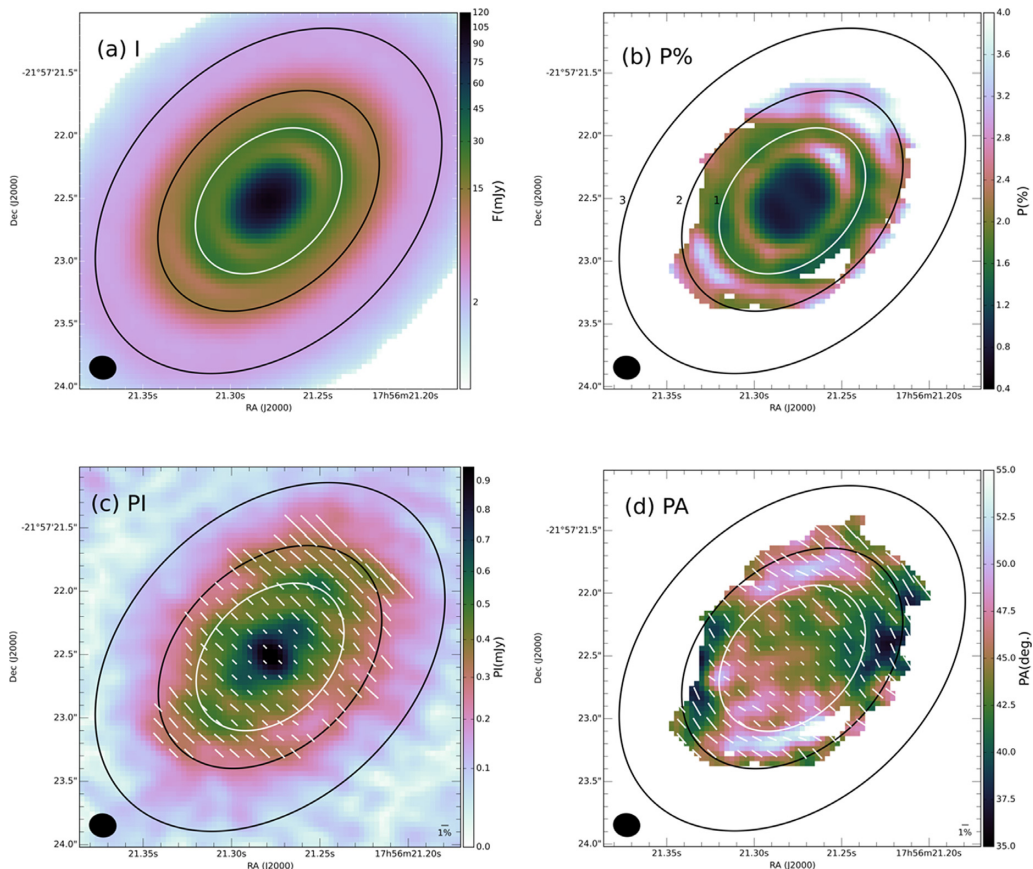


**Figure 1.** Sub-mm continuum polarization in HD163296. The top panels show (a) the total intensity and (b) the percentage polarization at band 7 in the central region. Superimposed as ellipses are representations of the three rings in the total intensity image, marked 1–3 in (b). The lower panels are (c) the polarized flux intensity and (d) the polarization angle, both with the polarization vectors superimposed. In (c), the vectors are shown at their actual angle, whereas in (d) the vector rotation relative to the mean of  $44.1^\circ$  is multiplied by a factor of 3, to emphasize the relative twist. Polarization fraction and angle are truncated at polarized flux levels of  $5\sigma$  per beam ( $250\mu\text{Jy}$ ). Images are 3 arcsec (315 au) across. Resolution is  $\sim 0.2$  arcsec (beams are shown lower left). Polarization vectors have  $1/2$  beam spacing, with lengths proportional to the polarization fraction.

sub-mm observations found an upper limit of 1 per cent to the polarization fraction in a 1 arcsec beam (Hughes et al. 2009). Pinte et al. (2018) and Teague et al. (2018) have also recently found dynamical evidence of massive planets in the system.

In this paper, we present ALMA observations of polarized dust emission of HD163296 at  $870\mu\text{m}$  with a resolution of  $\sim 0.2$  arcsec – sufficient to resolve the rings. We also combine the intensity images with archival band 6 data to obtain spectral index maps. The results are compared with a self-scattering model including the gaps and rings.

## 2 OBSERVATIONS

The observations were conducted in sessions on two nights: 2016 July 23 and August 13, with two consecutive executions of the scheduling block on each night and 35–37 antennas in the array. The polarization calibrator (J1751+0939) was observed every 30 min; J1742-2527 was used as a complex gain calibrator and observed every 7 min. J1733-1304 was used as a flux calibrator with assumed fluxes of 1.52 and 1.67 Jy at 343.5 GHz on the two observing nights; J1924-2914 was the bandpass calibrator. Checks showed that the independently calibrated fluxes of both the bandpass and polarization calibrators agreed with the measured values at that time from the ALMA online calibrator data base to better than 5 per cent.

The total time on-source was 2 h, although some 15 min of data were flagged in the second session while the target transited close to the zenith.

The system was set up to observe continuum in band 7 at a mean frequency of 343.5 GHz, with spectral windows at 336.494, 338.432, 348.494, and 350.494 GHz, each having 31.25 MHz channel spacing and 2 GHz nominal bandwidth, with a total usable bandwidth of 7.5 GHz.

The calibrated data from the ALMA pipeline were examined, further flagging applied, and the individual executions were used to create self-calibrated solutions for the antenna phase and amplitude. The polarization was then calibrated for each day separately, and the self-calibrated solutions applied. The two sessions were combined and imaged using CLEAN in CASA (McMullin et al. 2007), producing separate images of Stokes I, Q, U, and V. These were combined and debiased to give the polarized percentage  $P$  per cent =  $100\sqrt{Q^2 + U^2 - rms^2}/I$ , where  $rms$  is the noise in the Stokes Q and U images and  $I$  the total intensity. To maximize the signal/noise, natural uv weighting was applied, giving a beam of  $0.21 \times 0.19$  arcsec at  $81^\circ$ , and resulting in a final rms of  $\sim 50\mu\text{Jy}$  in the individual Stokes images.

To obtain the spectral index, we used the total intensity band 7 visibilities together with ALMA archive data taken in 2015 August in band 6 (originally published by Isella et al. 2016). Data were

combined using the multifrequency synthesis method (Rau & Cornwell 2011), which takes into account differences in the detailed uv coverage (although both data sets have a similar resolution, which minimizes such effects). A differential pointing offset of  $-11$ ,  $-73$  mas was measured (and corrected for). This may be partly due to the published stellar proper motion of  $-8$ ,  $-39$  mas, and partly from ALMA astrometric errors (typically 1/10 of the beam, or 20 mas). The resultant combined total intensity and spectral index images were obtained using CLEAN with Briggs robustness=0.5 uv weighting, to give a slightly higher resolution ( $0.18 \times 0.17$  arcsec), and an rms of  $55 \mu\text{Jy}$  at an effective central frequency of 291 GHz.

### 3 RESULTS

#### 3.1 Polarization

Images of the total intensity and polarization are shown in Fig. 1. These are derived from the individual Stokes data sets (see supplemental online data). The locations of the total intensity rings at radii of 67, 102, and 160 au are illustrated by the three superimposed circles inclined at  $45^\circ$  to the line of sight. The percentage polarization (Fig. 1b) ranges from 0.9 per cent in the centre, and increases up to  $\sim 4$  per cent at the edges along the major axis; beyond this the signal/noise of the polarized intensity drops below  $5\sigma$  (see Fig. 1c), making the fractional polarization uncertain. In the gaps between rings along the major axis, particularly between rings 1 and 2, the polarized intensity is relatively high compared with the total intensity, resulting in the regions of high fractional polarization (shown by lighter shading in Fig. 1b). This anticorrelation of polarization fraction and intensity is illustrated further in the major axis cross-cut in the upper panel of Fig. 2. Note that along the minor axis, the polarized flux is comparatively weak and only marginally detectable beyond ring 1 (Fig. 1c).

Figs 1(c)–(d) show a relatively constant polarization angle in the central bright region, with a median of  $44.1 \pm 1.5^\circ$  over the inner 30 au – closely aligned with the disc minor axis. However, there is a twist of up to  $\pm 9^\circ$  in the vectors at larger radii, most significant in the intensity gap between rings 1 and 2 (where the fractional polarization peaks). Here the vectors are more azimuthally aligned; this is more clearly illustrated when the offset in the angle relative to the central polarization is magnified (see Fig. 1d). This azimuthal twist can also be seen at smaller and larger radii in Fig. 1(d), albeit with a lower magnitude.

#### 3.2 Spectral index

The combined band 6+7 image of the spectral index,  $\alpha_{\text{mm}}$ , is shown in Fig. 3, with a cut along the major axis in Fig. 2(b). The increase in  $\alpha_{\text{mm}}$  with radius is consistent with Guidi et al. (2016), but now we can resolve dips in  $\alpha_{\text{mm}}$  at the ring peaks. These could be due to a local decrease in the dust emissivity slope  $\beta$ , or high optical depths in the rings. As their radial width is not resolved, the ring brightness temperature only provides a lower limit to the optical depth, so we cannot discriminate between these possibilities. The rings in HL Tau (ALMA Partnership et al. 2015) and TW Hya (Huang et al. 2018) also show lower  $\alpha_{\text{mm}}$ , which was associated with high optical depths.

In the central peak of HD163296,  $\alpha_{\text{mm}}$  is apparently as low as 1.4 – below that of isothermal blackbody emission in the Rayleigh–Jeans limit (2.0). Contribution from non-thermal emission is considered negligible at these wavelengths (Isella et al. 2007). The relative flux calibrations across each of the images are accurate to  $\leq 1$  per cent,

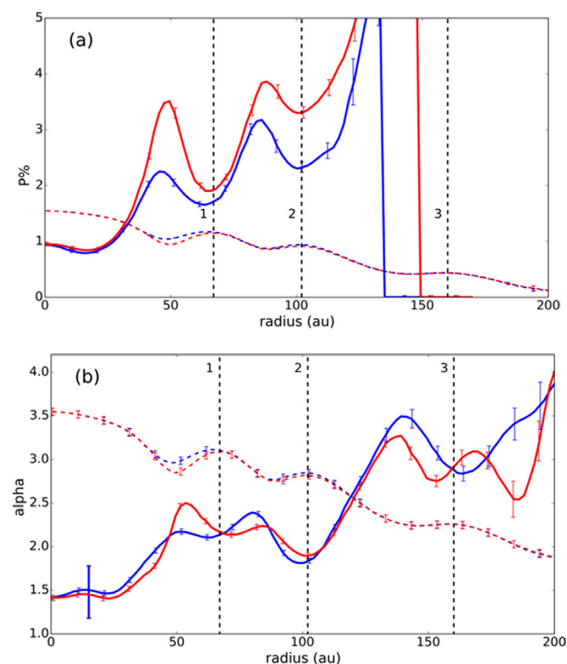


**Figure 2.** Sector cuts of polarization percentage ( $P$  per cent, upper panel) and spectral index  $\alpha$  (from band 6+7, lower panel) along the disc major axis. Data are the values along the major axis, averaged over arcs subtending an angle of  $-45 \pm 10^\circ$  on the sky (or deprojected  $\pm 14^\circ$  around the disc). Red and blue solid lines represent the NW and SE directions, respectively, from the central star. For a comparison, the dashed lines show the log of total intensity (arbitrary units) from the respective data sets. The radii of the three intensity rings are illustrated by the dotted vertical lines. Error bars are spaced by approximately one resolution element and depict the errors from random noise and image fidelity. The large error bar at lower left of the lower plot shows the systematic uncertainty in  $\alpha$  assuming 10 per cent calibration errors at the two wavelengths.

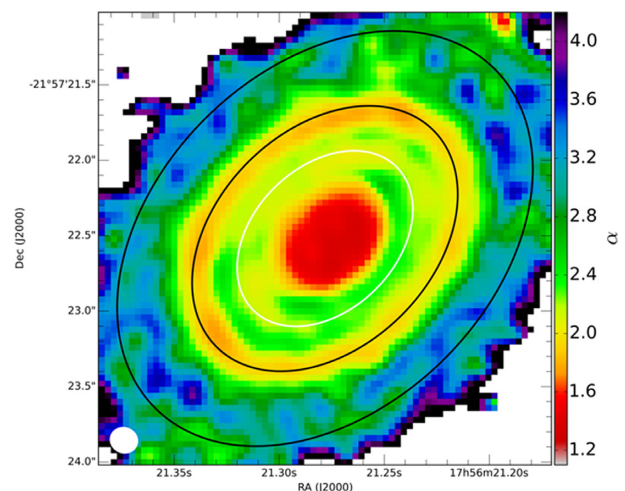


**Figure 3.** Spectral index map of HD163296. This is derived from the combined band 6 and 7 visibilities, with Briggs 0.5 weighting, resulting in a resolution of  $\sim 0.18$  arcsec. The positions of the three bright rings are shown by the ellipses.

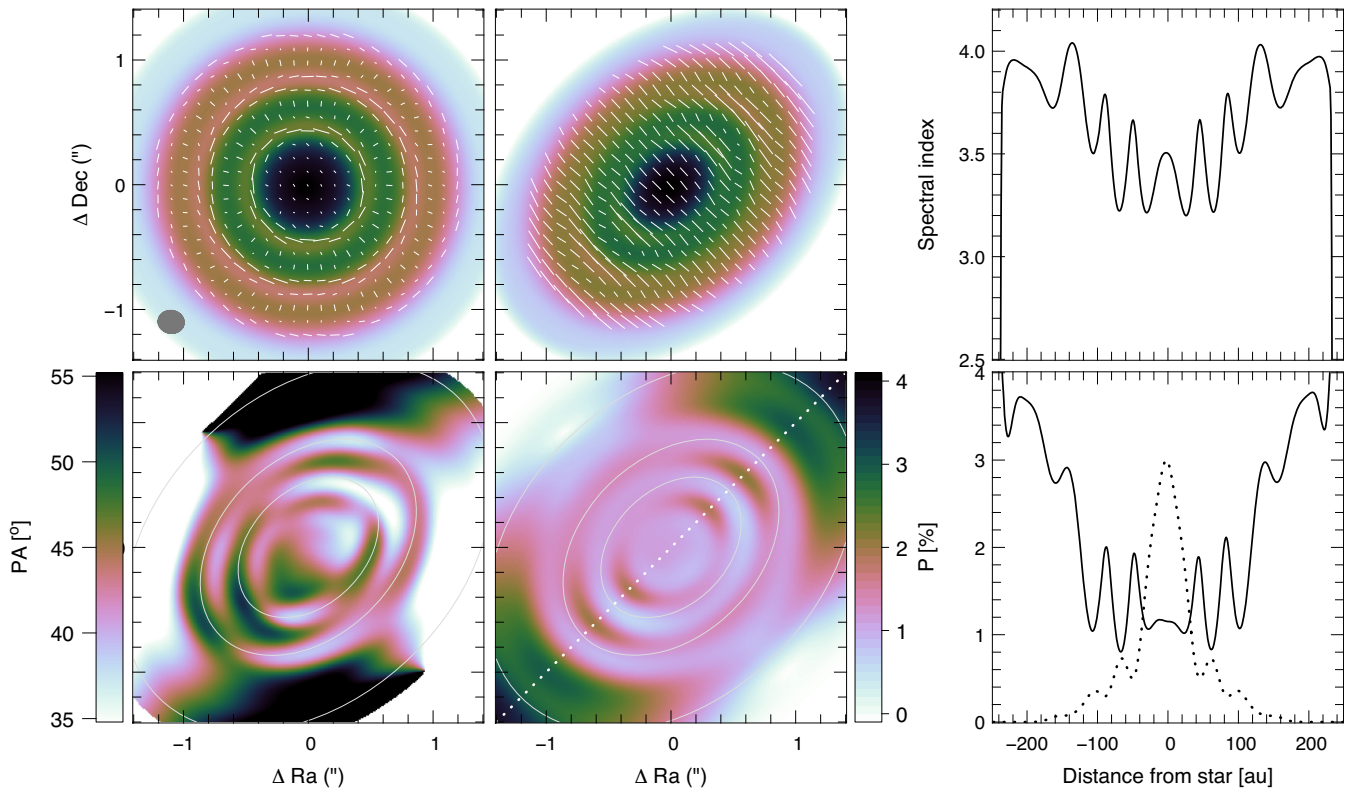


**Figure 4.** Sub-mm polarization produced by self-scattering in our *mcfost* model. *Top left*: pole-on model, the background image is the intensity convolved by the observed beam with polarization vectors overlaid. *Top centre*: same model at a  $45^\circ$  inclination. *Lower left and centre*: polarization angle and fraction. White ellipses mark the location of the bright intensity rings. 1 arcsec corresponds to 105 au. *Top right*: spectral index; *lower right*: polarization along the major axis, with intensity (arbitrary units) shown dotted.

so the profile of  $\alpha_{\text{mm}}$  in Fig. 2(b) is well determined. However, there may be an offset that depends on the absolute flux calibration in the two bands. A conservative calibration error is 7 per cent, which would correspond to a spectral index offset of 0.3, illustrated by the large error bar in Fig. 2(b). So while the relative shape of  $\alpha_{\text{mm}}$  in Fig. 2(b) is accurate, the range could change by  $\pm 0.3$ .

The total disc fluxes are 1.68Jy at band 7 and 0.70Jy at band 6, giving  $\alpha_{\text{mm}}$  of  $2.1 \pm 0.3$ . This is in reasonable agreement with that measured by Pinilla et al. (2014) ( $2.7 \pm 0.4$ ), but suggests an overall offset in  $\alpha_{\text{mm}}$ , marginally consistent with the formal flux uncertainty. Another possibility could be an  $\sim 20$  per cent decrease in luminosity in the interval between the band 6 and 7 observations. Alternatively, a hot core surrounded by cool optically thick dust may also reduce  $\alpha_{\text{mm}}$ , as proposed for some Class 0 objects (Li et al. 2017). Interestingly, TW Hya also showed  $\alpha_{\text{mm}} < 2.0$  in the centre, marginally inconsistent with the calibration accuracy (Huang et al. 2018).

#### 4 DISCUSSION AND MODELLING

The mm-wave polarization vectors in the central region of HD163296 are aligned within  $1.5^\circ$  of the disc minor axis. This alignment is similar to that seen in IM Lup (Hull et al. 2018), HL Tau at  $870 \mu\text{m}$  (Stephens et al. 2017) and CW Tau (Bacciotti et al. 2018), and is consistent with self-scattering in an inclined disc (Kataoka et al. 2016a; Yang et al. 2016b). Emission from non-spherical grains aligned either by magnetic or non-isotropic radiation fields can also give measurable mm polarization, but for inclined discs like HD163296, they do not predict the same vector orientation along

the minor axis in the centre (Yang et al. 2016b, 2017). At larger radii and in the gaps between the rings in HD163296, the polarization fraction increases and the vectors become more azimuthal. Can this also be explained by self-scattering alone?

To simulate scattering in a ringed system, we use the radiative transfer code MCFOST (Pinte et al. 2006, 2009), building a disc density model by inverting the intensity image with uniform CLEAN weighting into a surface density profile. We assume a passive disc with a  $28 L_\odot$  central stellar heating source and a Gaussian scale height of 10 au at 100 au (de Gregorio-Monsalvo et al. 2013). Details are outlined in Pinte et al. (2016) for HL Tau. Spherically symmetric dust grains are used, where the only source of polarization is scattering (multiple scattering is included). The corresponding Stokes Q and U maps are computed, and then convolved to the observed resolution (Fig. 4).

Polarization by scattering can reproduce the *general* features observed in the ALMA data. In particular:

- (i) The polarization is larger along the major axis, *i.e.* where the scattering angle is closer to  $90^\circ$ .
- (ii) The fractional polarization is anticorrelated with the intensity, with larger polarization inside the gaps (darker areas in Fig. 4, lower centre panel) (Kataoka et al. 2016a).
- (iii) The polarization vectors are aligned more with the disc minor axis in the central region and the intensity rings.
- (iv) The polarization angle displays a twist in the gaps, becoming more azimuthal (Fig. 4, left centre panel).

The twist in polarization angle in the gaps reflects the change in the scattering geometry and is more easily understood by looking

at the same model viewed pole-on (Fig. 4, top left). In the rings, the radiation field is mostly azimuthal, producing a radial polarization, while in the gaps, the radiation field is mostly radial, originating from the surrounding rings, resulting in an azimuthal polarization pattern (e.g. Kataoka et al. 2015, 2016a; Yang et al. 2016b). The discs around CW Tau (Bacciotti et al. 2018) and GGD27 (Girart et al. 2018) do not (yet) have resolved rings, but both show polarization alignment along the minor axis in the centre, with a more azimuthal orientation at larger radii. This was interpreted as a change in scattering geometry as the discs become optically thin further out. HD163296 has the same basic geometry, except there are multiple transitions between the optically thicker rings and optically thin gaps.

The polarized intensity is strongly dependent on the chosen grain model, and is affected by a combination of the dust albedo, scattering phase function, and polarizability phase function. We calculate dust optical properties using a distribution of hollow spheres with a maximum void fraction of 0.8. The model presented in Fig. 4 corresponds to compact astrosilicates (Draine 2003), with a maximum grain size  $a_{\max} \sim 100 \mu\text{m}$ , typical of that required to maximize the polarization (e.g. Kataoka et al. 2015, 2016a). This gives  $\alpha_{\text{mm}} \sim 3.5$  (larger in the optically thinner gaps, top right of Fig. 4), marginally consistent with HD163296 beyond a radius of 125 au. The low  $\alpha_{\text{mm}}$  at smaller radii may be explained by large (mm-sized) grains, but this is inconsistent with  $a_{\max}$  from the polarization (Yang et al. 2016a). This dichotomy may be explained if the inner rings are optically thick but radially unresolved. Alternatively  $\alpha_{\max}$  may depend on the vertical (or radial) location, with the  $100 \mu\text{m}$  grains on the surface (or in the gaps) and the mm dust in the mid-plane (or in the rings). In either case, the scattering geometry would not significantly change. Further dust modeling, together with observations with higher resolution and longer wavelengths may be able to reconcile the low  $\alpha_{\text{mm}}$  with the observed polarization fraction.

## ACKNOWLEDGEMENTS

This paper makes use of the following ALMA data: ADS/JAO.ALMA#2015.0.00616.S and #2013.0.00601.S. ALMA is a partnership of ESO (representing its member states), NSF (USA), and NINS (Japan), together with NRC (Canada), MOST and ASIAA (Taiwan), and KASI (Republic of Korea), in cooperation with the Republic of Chile. The Joint ALMA Observatory is operated by ESO, AUI/NRAO, and NAOJ. NRAO is a facility of the NSF operated under cooperative agreement by AUI. CP acknowledges funding from the Australian Research Council via FT170100040 and DP18010423. FM acknowledges funding from ANR of France via contract ANR-16-CE31-0013. Thanks to Satoshi Ohashi for comments on an earlier version of the results.

## REFERENCES

ALMA Partnership et al., 2015, *ApJ*, 808, L3  
 Bacciotti F. et al., 2018, *ApJ*, 865, L1  
 Cox E. G., Harris R. J., Looney L. W., Li Z.-Y., Yang H., Tobin J. J., Stephens I., 2018, *ApJ*, 855, 92

de Gregorio-Monsalvo I. et al., 2013, *A&A*, 557, A133  
 Draine B. T., 2003, *ARA&A*, 41, 241  
 Girart J. M. et al., 2018, *ApJ*, 856, L27  
 Guidi G. et al., 2016, *A&A*, 588, A112  
 Harris R. J. et al., 2018, *ApJ*, 861, 91  
 Huang J. et al., 2018, *ApJ*, 852, 122  
 Hughes A. M., Wilner D. J., Cho J., Marrone D. P., Lazarian A., Andrews S. M., Rao R., 2009, *ApJ*, 704, 1204  
 Hull C. L. H. et al., 2018, *ApJ*, 860, 82  
 Isella A., Testi L., Natta A., Neri R., Wilner D., Qi C., 2007, *A&A*, 469, 213  
 Isella A. et al., 2016, *Phys. Rev. Lett.*, 117, 251101  
 Kataoka A. et al., 2015, *ApJ*, 809, 78  
 Kataoka A., Muto T., Momose M., Tsukagoshi T., Dullemond C. P., 2016a, *ApJ*, 820, 54  
 Kataoka A. et al., 2016b, *ApJ*, 831, L12  
 Kataoka A., Tsukagoshi T., Pohl A., Muto T., Nagai H., Stephens I. W., Tomisaka K., Momose M., 2017, *ApJ*, 844, L5  
 Lee C.-F., Li Z.-Y., Ching T.-C., Lai S.-P., Yang H., 2018, *ApJ*, 854, 56  
 Li J. I., Liu H. B., Hasegawa Y., Hirano N., 2017, *ApJ*, 840, 72  
 McMullin J. P., Waters B., Schiebel D., Young W., Golap K., 2007, in Shaw R. A., Hill F., Bell D. J., eds, *ASP Conf. Ser. Vol. 376, ADASS XVI*. Astron. Soc. Pac., San Francisco, p. 127  
 Monnier J. D. et al., 2017, *ApJ*, 838, 20  
 Montesinos B., Eiroa C., Mora A., Merín B., 2009, *A&A*, 495, 901  
 Muro-Arena G. A. et al., 2018, *A&A*, 614, A24  
 Pinilla P. et al., 2014, *A&A*, 564, A51  
 Pinte C., Ménard F., Duchêne G., Bastien P., 2006, *A&A*, 459, 797  
 Pinte C., Harries T. J., Min M., Watson A. M., Dullemond C. P., Woitke P., Ménard F., Durán-Rojas M. C., 2009, *A&A*, 498, 967  
 Pinte C., Dent W. R. F., Ménard F., Hales A., Hill T., Cortes P., de Gregorio-Monsalvo I., 2016, *ApJ*, 816, 25  
 Pinte C. et al., 2018, *ApJ*, 860, L13  
 Rau U., Cornwell T. J., 2011, *A&A*, 532, A71  
 Stephens I. W. et al., 2017, *ApJ*, 851, 55  
 Tazaki R., Lazarian A., Nomura H., 2017, *ApJ*, 839, 56  
 Teague R., Bae J., Bergin E. A., Birnstiel T., Foreman-Mackey D., 2018, *ApJ*, 860, L12  
 Yang H., Li Z.-Y., Looney L., Stephens I., 2016a, *MNRAS*, 456, 2794  
 Yang H., Li Z.-Y., Looney L. W., Cox E. G., Tobin J., Stephens I. W., Segura-Cox D. M., Harris R. J., 2016b, *MNRAS*, 460, 4109  
 Yang H., Li Z.-Y., Looney L. W., Girart J. M., Stephens I. W., 2017, *MNRAS*, 472, 373  
 Zhang K., Bergin E. A., Blake G. A., Cleeves L. I., Hogerheijde M., Salinas V., Schwarz K. R., 2016, *ApJ*, 818, L16

## SUPPORTING INFORMATION

Supplementary data are available at [MNRAS](https://academic.oup.com/mnras/article/482/1/L29/5107365) online.

### Appendix A. Polarization Images.

Please note: Oxford University Press is not responsible for the content or functionality of any supporting materials supplied by the authors. Any queries (other than missing material) should be directed to the corresponding author for the article.

This paper has been typeset from a  $\text{\TeX}/\text{\LaTeX}$  file prepared by the author.